Microwave Device Characterization Using a Widefield Diamond Microscope

Andrew Horsley,[1,2,*] Patrick Appel,[1] Janik Wolters,[1] Jocelyn Achard,[3] Alexandre Tallaire,[3]
Patrick Maletinsky,[1,†] and Philipp Treutlein[1]

[1]*Departement Physik, Universität Basel, Basel CH-4056, Switzerland*
[2]*Laser Physics Centre, Research School of Physics and Engineering, Australian National University, 2601
Canberra, Australia*
[3]*Laboratoire des Sciences des Procédés et des Matériaux (LSPM), CNRS, Université Paris 13, Sorbonne Paris
Cité, 99 avenue J.B. Clément, 93430 Villetaneuse, France*

Devices relying on microwave circuitry form a cornerstone of many classical and emerging quantum technologies. A capability to provide *in-situ*, noninvasive, and direct imaging of the microwave fields above such devices would be a powerful tool for their function and failure analysis. In this work, we build on recent achievements in magnetometry using ensembles of nitrogen-vacancy centers in diamond, to present a widefield microwave microscope with few-micron resolution over a millimeter-scale field of view, $130 \text{ nT Hz}^{-1/2}$ microwave-amplitude sensitivity, a dynamic range of 48 dB, and submillisecond temporal resolution. We use our microscope to image the microwave field a few microns above a range of microwave circuitry components, and to characterize an alternative atom-chip design. Our results open the way to high-throughput characterization and debugging of complex multicomponent microwave devices, including real-time exploration of device operation.

Microwave (MW) devices play a critical role in telecommunications, defence, and quantum technologies. Device characterization via high-resolution MW field imaging is a long-standing goal [1–3], which promises to overcome the limitations of conventional characterization techniques. For example, it is difficult to identify internal features of complex devices using S-parameter measurements of reflection and transmission through external device ports [4,5]. A high-throughput MW-imaging method would allow for fast prototype iteration and for more adventurous development of novel device architectures. Furthermore, MW imaging is of interest for spin-wave imaging in magnonic systems [6,7], is under investigation for medical imaging [8,9], and can be used to characterize materials [10] and biological samples [11]. In recent years, alkalivapor cells with atoms in the ground [12–16] or highly excited Rydberg [17–19] states, and nitrogen-vacancy (NV) centers in diamond [20–23] have shown promise for intrinsically calibrated MW imaging in simple vacuum-free and cryogen-free environments. Ensembles of NVs in a widefield diamond microscope [24–28] provide an excellent balance between the sensitivity and wide field of view (FOV) offered by vapor cells and the nanoscale spatial resolution of single NV centers [29] and so far have been primarily employed for imaging static and low-frequency magnetic fields. In this work, we demonstrate high-throughput widefield diamond microscopy for MW device characterization, enabled by a step change that we have achieved in microscope performance.

Our microscope integrates advances in camera speed, experiment control, recently developed diamond material, laser illumination, and the use of an intrinsically calibrated MW-sensing scheme to perform MW imaging with an unprecedented combination of temporal resolution, FOV, and spatial resolution. We demonstrate an approximately 0.5 mm^2 FOV with few-micron spatial resolution, a MW-amplitude sensitivity of $130 \text{ nT Hz}^{-1/2}$, and a dynamic range of 48 dB. We have advanced the temporal resolution to the submillisecond regime, an order of magnitude beyond the previous state of the art [22], enabling dynamic probing of circuit operation and real-time exploration of large-scale devices by scanning them under the microscope (Movies 1 and 2 in Supplemental Material (SM) [30]). In addition, the accessible design of our microscope enables high-throughput measurements with rapid exchange of MW devices, demonstrating its applicability to industry-relevant environments.

I. MICROWAVE IMAGING WITH THE WIDEFIELD DIAMOND MICROSCOPE

Our imaging goal is to determine the spatial profile of an inhomogeneous MW field of known frequency. We

---

*andrew.horsley@unibas.ch
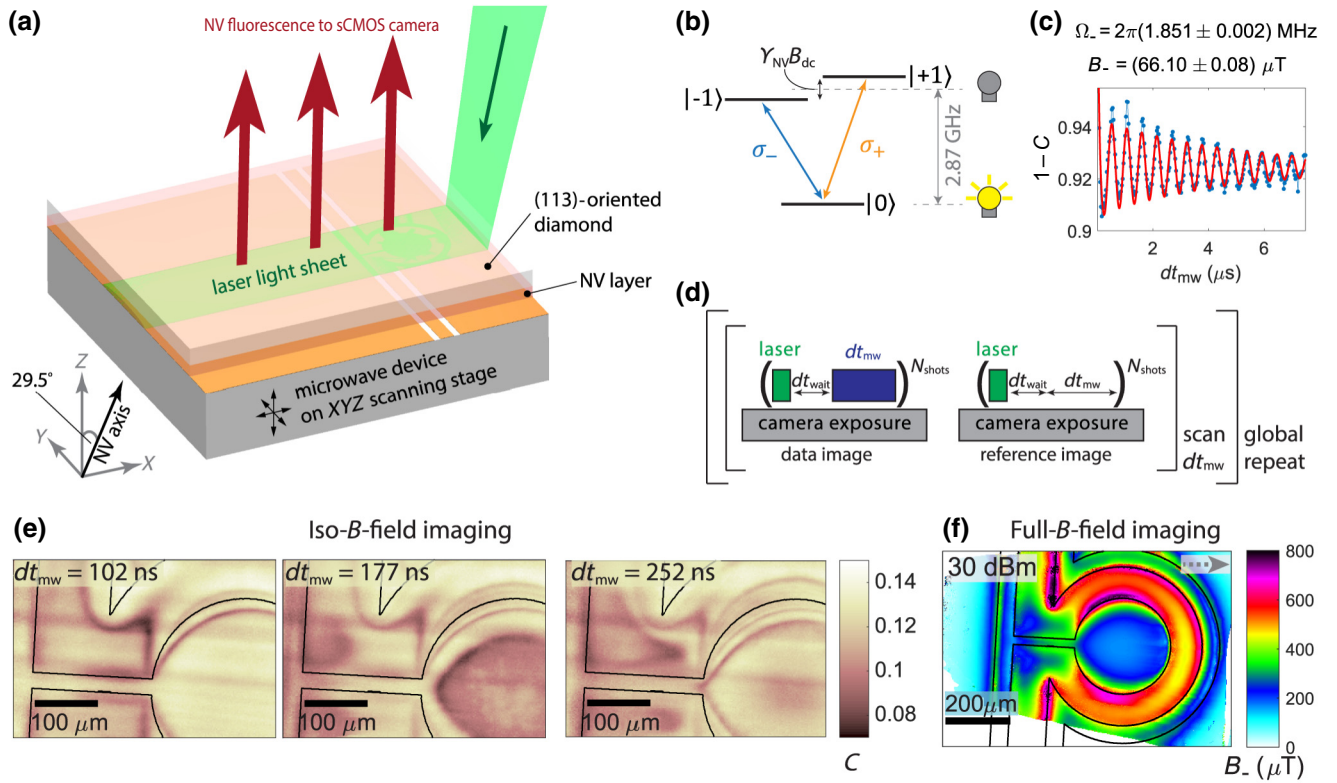†patrick.maletinsky@unibas.ch

FIG. 1. The widefield diamond microscope and MW-imaging technique. (a) A schematic of the MW-imaging setup. We perform imaging using NVs aligned along the (111) axis, tilted $29.5°$ from the vertical in the X-Z plane. (b) The NV-center ground-state-level structure, showing the $\sigma_\pm$ polarized MW transitions. (c) Rabi oscillations driven by a MW magnetic field between bright ($|0\rangle$) and dark ($|+1\rangle$ or $|-1\rangle$) fluorescing states. A fit using Eq. (1) is shown in red. (d) The full-B-field imaging sequence. (e) The iso-B-field imaging mode, revealing the contours of the MW magnetic field. Images are shown for MW pulses of varying length (dt_{MW}). Horizontal streaks are due to spatial variation in the 532 nm laser intensity. (f) A full-B-field image, obtained from a sequence of iso-B-field images where dt_{MW} is scanned, yielding a time-domain Rabi oscillation signal for each pixel [as shown in (c)]. Pixelwise fitting then yields an image of the MW magnetic field. sCMOS, scientific complementary metal-oxide-semiconductor.

perform measurements by driving oscillations on an NV MW transition and measuring the oscillation frequency, which is proportional to the MW magnetic-field amplitude. At the core of our microscope is a diamond containing a high-density layer of NV centers that can be brought into close proximity to a MW device [Fig. 1(a)]. In our particular setup, we use a (113)-oriented diamond with an approximately 25-μm-thick high-density (4×10^{14} cm^{-3}) layer of NV centers preferentially oriented along the (111) axis, i.e., oriented at a $29.5°$ angle from the diamond surface normal (see SM Note 1 [30]; see also Ref. [31]). NV centers are optically active lattice defects in diamond, with an electronic spin-1 ground state [Fig. 1(b)] [32,33]. Excitation with 532 nm laser light stimulates state-dependent fluorescence, and pumps the NV population into the brightly fluorescing $|0\rangle$ state. To optimize the FOV for a given laser power, we excite the NVs using an in-plane sheet of 532 nm laser light [Fig. 1(a); see SM Note 1 [30]]. The $|0\rangle$ state is coupled to the darker $|\pm 1\rangle$ states by MW magnetic-dipole transitions. To detect MW fields, we first apply a dc magnetic field (B_{dc}) to tune one of the ground-state MW

transitions into resonance with the MW frequency of interest. Using an appropriate pulse sequence (see below), we then measure the coherent Rabi oscillations driven by the MW between the coupled states, from which we extract the Rabi frequency [Fig. 1(c)] [20,34]. The measurements resolve the MW polarization, as each transition is sensitive to only a single polarization component of the MW magnetic field, $B_\pm$ for the respective $\sigma_\pm$ ($|0\rangle \rightarrow |\pm 1\rangle$) transitions, with the polarization quantization axis parallel to the NV axis (see SM Note 1 [30]). A single NV axis can be used to measure both B_+ and B_- at a given frequency, by reversing the B_{dc} direction in turn to tune each of the $\sigma_\pm$ transitions to the desired resonance frequency. Our measurements are intrinsically calibrated, as the Rabi oscillation frequency, $\Omega_\pm$, is related to the MW amplitude by $B_\pm = \Omega_\pm/(2\pi \gamma_{NV})$, through the well-characterized NV gyromagnetic ratio, $\gamma_{NV} = 28$ kHz/μT.

We perform imaging by taking a series of data and reference images [Fig. 1(d)]. The data-image sequence consists of a single (700 ns) laser pulse, followed by a single MW pulse input to the MW device under test (DUT). A wait
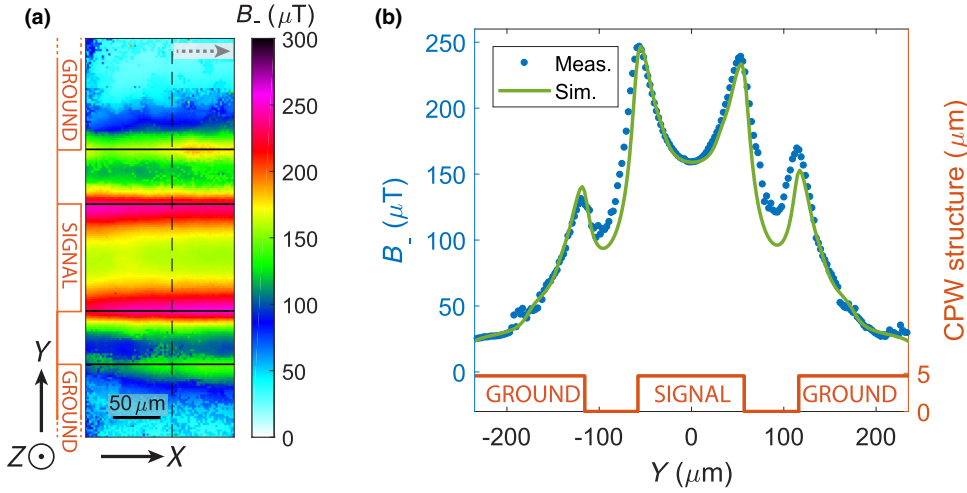
FIG. 2. A validation measurement on a section of coplanar waveguide (CPW). (a) The measured MW field, B_-, with an input power to the chip of 22.6 dBm. Horizontal black lines outline the CPW structure. The NV axis is oriented 29.5° from the Z axis, in the direction of the X axis, as indicated by the dashed gray arrow. (b) A line cut through the CPW [indicated by a dashed line in (a)], compared to simulation.

time of $dt_{\text{wait}} = 1.5$ μs between the laser and MW pulses allows for relaxation of the optically excited NV electron through a metastable state. This sequence is repeated $N_{\text{shots}} \approx 100$ times during a single camera exposure to accumulate fluorescence counts. The laser pulse both reads out the state of the NVs after the previous MW pulse and prepares the NVs in the $|0\rangle$ state before the next MW pulse. We then take a reference image, with a sequence identical to the data image, but with the MW off. The data and reference images are combined pixelwise to create a contrast image of the relative change in fluorescence induced by the MW pulse, $C = 1 - N_{\text{data}}/N_{\text{ref}}$, where N_{data} (N_{ref}) is the fluorescence counts for a given data (reference) pixel. The use of a reference image reduces the sensitivity to spatial variation in fluorescence collection efficiency and noise (e.g., temporal laser intensity fluctuations) slower than the approximately millisecond separation of the data and reference images, limited by the camera frame rate. However, as we operate below the NV optical-saturation level, spatial variation in laser intensity does result in variation in the initialization fidelity of NVs in the $|0\rangle$ state and a proportional variation in contrast.

We operate in either of two imaging modalities: iso-B-field and full-B-field imaging [21,34]. Iso-B-field imaging [Fig. 1(e)] is a single-shot technique, providing the highest temporal resolution. We drive Rabi oscillations for a fixed duration, dt_{MW}, leaving NV centers in a superposition of bright and dark states depending on the local $B_\pm$. Bright lines in the fluorescence contrast images occur at $\Omega_\pm = m\pi/dt_{\text{MW}}$, where m is an integer, and therefore follow the contour lines of $B_\pm$. Longer dt_{MW} pulses drive more Rabi oscillations, resulting in more closely spaced contour lines and a higher MW-amplitude resolution. Calibration of the contour lines can be performed by counting them from a region far from the MW source (where $B_\pm \sim 0$), inward toward the MW source [34]. Although fast, iso-B-field images can be obscured by contrast variation due to,

e.g., inhomogeneous laser illumination [the cause of the horizontal stripes in Fig. 1(e)] and are limited in MW-amplitude resolution by the optical imaging resolution and MW-amplitude gradient [21].

Full-B-field imaging [Fig. 1(f)] extends the iso-B-field technique by scanning dt_{MW}. This gives a time-varying signal for each pixel in an image [Fig. 1(c)], from which we extract the Rabi frequency using the fit function

$$y = A - \Big[B\exp(-dt_{\text{MW}}/\tau_{\text{fast}})$$
$$+ C\exp(-dt_{\text{MW}}/\tau_{\text{slow}})\Big]\sin(\Omega_\pm dt_{\text{MW}}), \qquad (1)$$

where A, B, C, τ_{fast}, τ_{slow}, and $\Omega_\pm$ are fit parameters. Details of the fitting are discussed in SM Note 2 [30]. By directly measuring an oscillation frequency, our measurements become largely insensitive to spatial and temporal fluctuations in signal amplitude, and the $B_\pm$ amplitude resolution becomes limited only by the contrast detection noise. We demonstrate a 48 dB dynamic range in MW power (see SM Note 1 [30]), with the lower bound given by the NV coherence time in our diamond sample and the upper bound given by the available MW power.

The microscope can be readily adjusted to optimize temporal resolution, dynamic range, field of view, sensitivity, or spatial resolution, as discussed in SM Note 1 [30]. The DUT is mounted separately to the diamond, meaning that it can be scanned to build up composite images of arbitrary size. The MW images presented in this work (Figs. 2–4) required 2–3 min of measurement time per image at a given DUT position. Separate DUT mounting and the open geometry of the microscope allow for high-throughput MW device characterization, with DUT exchange and realignment a straightforward process that can be performed in under 10 min.
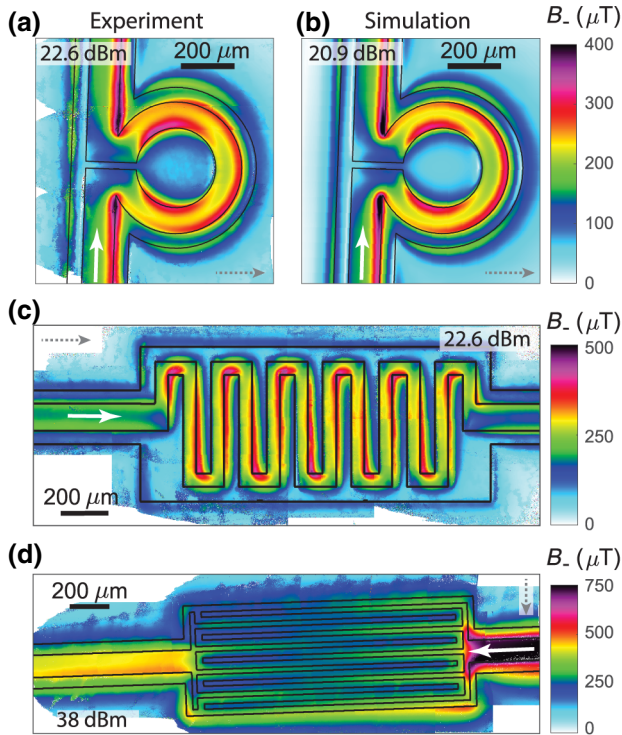
FIG. 3. Images of 2.77 GHz MW near fields above various lumped-element structures. The measured (a) and simulated (b) field above an omega resonator. (c) The measured field above a meander line. (d) The measured field above an interdigital capacitor. The solid white arrows indicate the direction of MW propagation, the dashed gray arrows indicate the projection of the NV axis onto the X-Y plane, and the solid black lines show the contours of the DUT structures. The MW powers, given in dBm, are measured immediately before the input to the devices. The MW images for each structure are each stitched together from several smaller overlapping images.

II. MICROWAVE DEVICE CHARACTERIZATION

We first validate our MW imaging system by measuring the field above a section of coplanar waveguide (CPW) and comparing our results to simulation. The CPW has a 120-μm-wide central signal line, with 54 μm gaps to ground planes on either side (see SM Note 1 [30]). Figure 2(a) shows the measured B_- component of the MW magnetic field at 2.77 GHz. We use the SONNET software to simulate the two-dimensional (2D) MW current distribution in the CPW (SM Fig. S5a [30]). We then calculate the resulting MW magnetic near field using the Biot-Savart law, and determine the B_- projection onto the NV axis. To account for the finite sensing volume, we integrate the field over a range $Z = h \pm d/2$ above the CPW. The mean sensing height, h, is a fit parameter, while the sensing layer thickness, $d = 14$ μm, is given by the thickness of the laser light sheet (see SM Note 1 [30]). Figure 2(b) compares the measured and simulated fields in a line cut across

the CPW. We find good agreement with $h = 12$ μm and a MW current in the signal line of $J_{\mathrm{MW}} = 50$ mA, without additional free fit parameters. Assuming that the laser light sheet extends to the edge of the diamond, this corresponds to a chip-diamond separation of $h - d/2 = 5$ μm. The simulated MW power is $P_{\mathrm{MW}} = J_{\mathrm{MW}}^2 Z = 20.9$ dBm, where $Z \approx 50$ Ω is the waveguide impedance, corresponding to a 1.7 dB insertion loss of the measured 22.6 ± 2 dBm input power.

Figures 3(a) and 3(b) show the measured and simulated B_- component of the MW field above an omega-loop resonator, a structure often used to produce uniform MW fields for the control of quantum systems [35]. We see excellent agreement between the measured and simulated fields if we impose an asymmetric drive of the structure. That is, we perform the simulation using an asymmetric current distribution between the CPW signal line and each of the ground planes, with a current-imbalance of about 30% between the left and right sides of the CPW signal line (see SM Fig. S5b [30]). By exploring the MW field in the CPW upstream from the omega loop (see SM Movie 1 [30]), we can gain an understanding of the origin of this asymmetric current. Upstream of a 90° bend in the CPW, the B_- profile is symmetric (SM Fig. S5c [30]), and is well matched by fields produced by the same symmetric current distribution used in Fig. 2(b). However, the MW field distribution after the bend (measured immediately before the omega loop) is best matched by fields produced by the asymmetric current distribution (SM Fig. S5d [30]). We can therefore conclude that the asymmetric current is likely induced by either the CPW bend or by reflections from any impedance mismatch between the omega loop and the CPW. In addition to the field asymmetry produced by the MW current asymmetry, the B_- asymmetry above the CPW downstream of the 90° bend is also due to the angle between the MW current and the NV axis.

As a demonstration of the versatility of the microscope, we then image B_- above an inductive meander line [Fig. 3(c)] and an interdigital capacitor [Fig. 3(d)]. As in the omega loop, we see that the MW field, and therefore the current, is largely confined to edge modes, but avoids the outer edges of corners. In Fig. 3(c), the field features of the meander become blurred toward the left of the image, due to a 0.25° tilt between the diamond and chip increasing the mean sensing distance from $h = 11$ μm on the right-hand side of the image, to $h = 20$ μm on the left-hand side. In Fig. 3(d), we see that the majority of the MW current is reflected at the CPW-capacitor interface. To increase the signal in the capacitor fingers, we input a relatively large $P_{\mathrm{MW}} = 38$ dBm. The image shows that capacitive coupling does indeed transfer some MW current from the upstream to downstream fingers; however, a significant current bypasses the capacitor fingers, flowing the through the ground planes surrounding the finger structure.
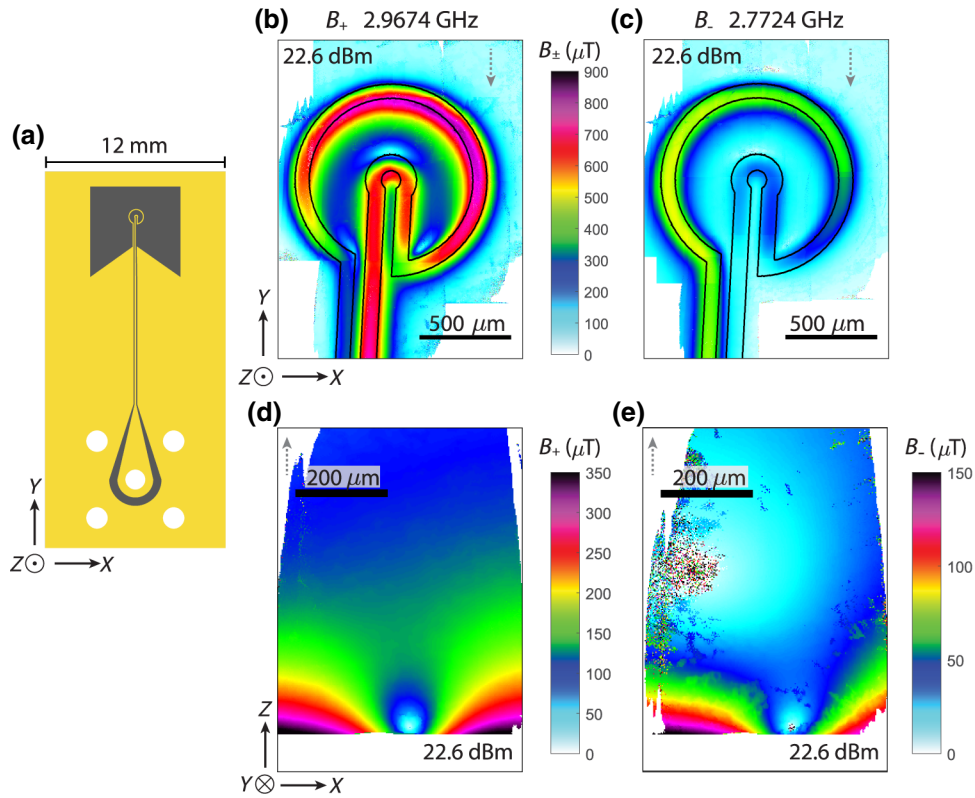
FIG. 4.   The prototype atom chip, producing an all-MW trapping potential. (a) A schematic of the trap chip, with metallization shown in yellow, the etched surface in gray, and through holes for a SubMiniature version A (SMA) jack in white. (b),(c) The MW field measured in the X-Y plane above the chip, at a MW frequency near a resonance of the chip [(b), 2.9674 GHz] and off resonance [(c), 2.7724 GHz]. (d),(e) The MW field measured in the X-Z plane above the chip, near resonance [(d), 2.9674 GHz] and off resonance [(e), 2.7724 GHz]. The dashed gray arrows indicate the projection of the NV axis onto the X-Y plane (b),(c) or the X-Z plane (d),(e), and the solid black lines show the contours of the trap-chip structure. Images (b) and (c) are composites stitched together from several smaller images, while (d) and (e) show a single imaging position. The particular mounting of the NV diamond limits the distance of approach to 80 μm above the chip surface in (c) and (e), as indicated by the white space below each MW image.

In Fig. 4(a), we present a prototype design of an atom chip, which is a type of device used for trapping and manipulating ultracold atoms, and a key platform for practical applications of quantum technologies that exploit such atoms [36]. We use our microscope to perform an initial characterization, confirming that the chip provides an all-MW trapping potential, an addition to the atom-chip toolbox that will enable, e.g., chip-generated trapping of atoms in hyperfine states untrappable using static fields [37,38]. The trapping potential, a minimum in the MW field above the chip, is created by counterpropagating MW currents through the inner and outer loops of a stripline. The chip is a single-port device, with a CPW transitioning into the stripline used to form the trapping geometry, which then terminates to the ground plane.

We probe the chip at two frequencies, near and away from a resonance (identified using S-parameter measurements; see SM Fig. S6 [30]). Near the resonance, at 2.9674 GHz, Fig. 4(b) shows the B_+ field in the X-Y plane above the trapping section. The MW field is reproducible in

SONNET simulations (SM Fig. S7 [30]) by adjusting the relative impedances of the input and output ports at either end of the stripline [our simulations only consider the structure within the field of view of Fig. 4(b)] to produce a gradual attenuation of $|J_{MW}|$ through the loops. This smooth evolution of current implies that the resonance feature is not a resonance of the trapping loops, but is likely a resonance of the entire chip. In Fig. 4(d), we probe the chip away from the resonance, at 2.7724 GHz. This time, we image the B_- component of the field, but due to the confinement of current flow in the stripline, we can reasonably expect that the MW field is close to linearly polarized and so $|B_-| \approx |B_+|$ (for a measured example and discussion, see SM Note 3 and SM Fig. S11 [30]). As we might expect, the off-resonant field in Fig. 4(d) is weaker than the field on resonance in Fig. 4(b), with a factor-of-2 reduction in the maximum measured field. A more surprising feature is the change in the spatial mode of the off-resonant field. We are unable to conclusively determine the cause of this mode change within the scope of this work.

The field distribution perpendicular to the chip, which we can image by mounting the chip perpendicular to the diamond, is particularly useful for characterizing the trapping potential and Fig. 4(d) shows the B_+ component of a 2.9674 GHz MW field in the X-Z plane. Note, however, that the change in chip-diamond orientation results in $\theta = 90°$ rotation of the NV axis with respect to the chip coordinate system and a corresponding change in the definition of B_+. Figure 4(d) shows that a tight trapping potential is formed 100 μm above the chip, with a Z axis gradient of 3.7 (2.2) μT μm^{-1} below (above) the trap and a symmetric X axis gradient of 2.7 μT μm^{-1}. We investigate the frequency dependence of the trapping field in Fig. 4(e), where we image the B_- component of a 2.7724 GHz field. We again see a trapping potential 100 μm above the chip. The field and trap gradients are 2–3 times lower than in Fig. 4(d), matching the weaker fields seen off resonance in Fig. 4(c), and the trap position is shifted by $\Delta X = +40$ μm, qualitatively matching the asymmetry along X in Fig. 4(c) compared to Fig. 4(b). In future versions of the chip, it may be possible to take advantage of this to scan the trap position by changing the input MW frequency (adjusting both the atoms' resonant frequency with a dc magnetic field and P_{MW} as necessary). A second, broad minimum, the origin of which is unclear, also appears in Fig. 4(e), 430 μm above the chip surface.

The surprising features of the measured MW field distributions on the structures in Figs. 3 and 4 underline the importance of performing high-resolution MW field measurements. Our imaging method is ideally suited for this task, as it provides calibrated images, which are well reproduced by simulations on simple structures such as the coplanar waveguide in Fig. 2. The detailed interpretation of the observed field distributions on more complex circuits such as in Figs. 3 and 4 will require further dedicated studies of MW propagation on these structures.

III. TEMPORAL RESOLUTION

We achieve our highest temporal resolution in the iso-B-field imaging mode, with reference images taken offline. The temporal resolution in our current system is ultimately limited by the camera frame rate, which is proportional to the number of pixel rows read out. Reading out 360 columns and 200 rows, corresponding to a 850×470 μm^2 field of view, and choosing $N_{\text{shots}} = 50$ shots per exposure, we achieve a temporal resolution of 2.2 ms. We demonstrate this approximately kilohertz frame rate in Figs. 5(a) and 5(b), where we measure a pulse train with a 5 ms on-off cycle. Each pixel in Fig. 5(a) provides a similar time-trace signal to that shown in Fig. 5(b). To explore our ability to detect externally controlled signals, we use an independent pulse generator to switch a $P_{MW} = 22.6$ dBm, 2.77 GHz signal. The imaging sequence is identical to the reference image sequence in Fig. 1(d), but with a fixed gap between laser pulses of $dt_{\text{wait}} + dt_{\text{MW}} = 530$ ns. Reducing the readout to 50 rows further improves the temporal resolution to 0.7 ms, as shown in Fig. 5(c), where we measure
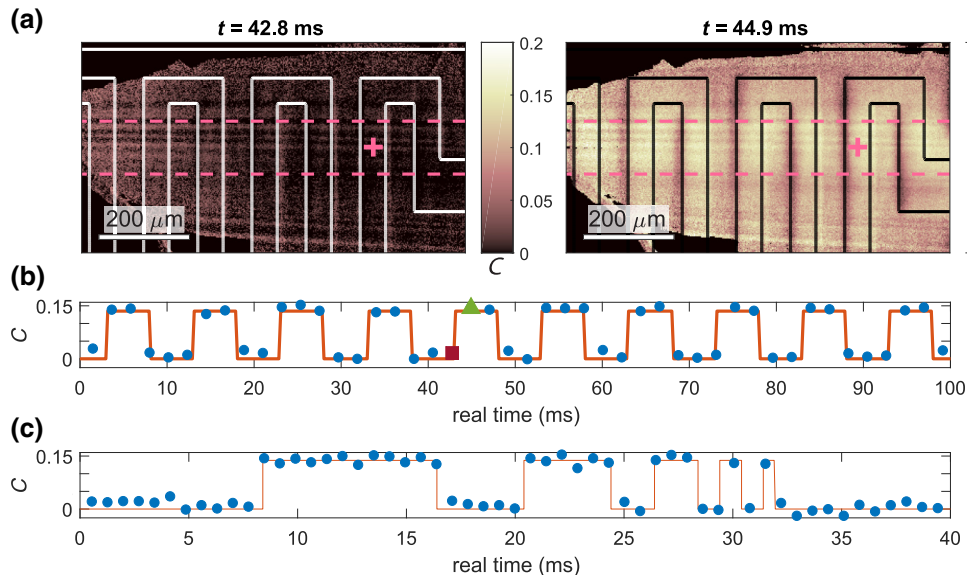

FIG. 5. A demonstration of temporal resolution in the iso-B-field imaging mode. (a) Iso-B-field images of B_- above a section of the meander line chip, with a 2.77 GHz MW signal off (left) and on (right). The full vertical field of view is 200 pixel rows. The horizontal dashed lines indicate the field of view for 50 rows. The meander structure is outlined in white. (b) A time trace for the pixel denoted by a pink cross in (a), as a MW signal is pulsed on and off. The time steps corresponding to the example images are indicated by a red square (MW off) and a green triangle (MW on). (c) A time trace with 50 pixel rows read out, showing submillisecond temporal resolution.
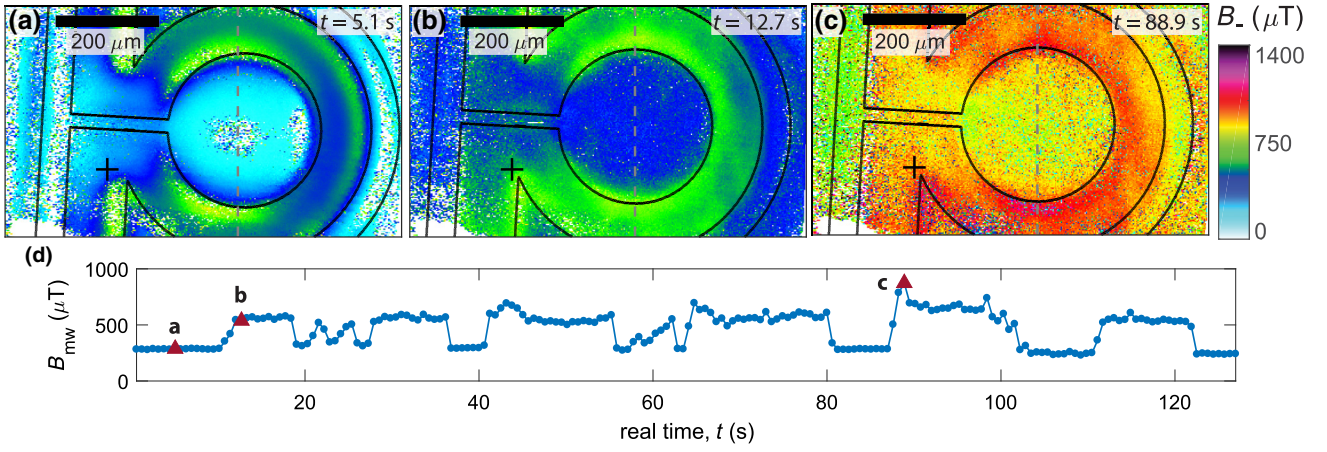
FIG. 6.   Full-B-field MW imaging at a 1.6 Hz rate. (a)–(c) Frames from SM Movie 2 [30], showing the B_- component of a 2.77 GHz MW field above the omega loop as the pins of the device input port are shorted to one another: (a) corresponds to the unperturbed device. The MW field profiles along the vertical gray dashed lines are given in SM Fig. S8 [30]. (d) The time trace for the pixel indicated by black crosses in the images in (a)–(c). The red triangles indicate the times of the frames shown in (a)–(c).

a train of pulses between 8 and 0.5 ms in length. The measurements in Fig. 5 use a short sensing time, of $dt_{MW} = 30$ ns. However, longer sensing periods (e.g., 1–10 μs), which would provide images with richer contour lines, can be used without loss of temporal resolution, as the frame rate is dominated by camera readout.

To combine full-B-field imaging with high bandwidth, we perform fast scans of dt_{MW}, with an experiment sequence identical to that used for the images in Figs. 3 and 4, but with only a single global repeat. There is a trade-off between the temporal resolution and the dynamic range, through the choice of the number of dt_{MW} steps. We choose a 100-timestep sequence, and perform full-B-field B_- imaging with a 1.6 Hz frame rate, using $N_{shots} = 195$ shots per exposure, 200 pixel rows, and with reference images taken online. This imaging mode allows for an intuitive exploration of devices and MW near fields, as demonstrated in SM Movie 1 [30], where we scan the omega-loop chip to explore MW fields upstream of the loop. Figure 6 shows frames and a pixel time trace from a second movie taken of the omega-loop chip (SM Movie 2 [30]), where we deliberately perturb the MW current modes by periodically shorting the signal and ground pins of the MW input port. We see the MW amplitude and spatial mode change dramatically as we change the spatial mode and efficiency of MW launch into the device. Figures 6(b) and 6(c) show improved MW field homogeneity and strength in the center of the omega loop, compared to the unperturbed case in Fig. 6(a) (see also profiles of the fields in SM Fig. S8 [30]). This highlights a perhaps rarely considered degree of freedom in experimentally optimizing devices, where one could envisage, for example, optimizing a device for manipulating quantum systems by shorting the input port pins in a controlled manner.

IV. CONCLUSIONS AND OUTLOOK

We present a widefield diamond microscope based on NV centers and demonstrate its substantial potential for characterizing MW devices. Our submillisecond temporal resolution represents an order-of-magnitude improvement over the previous approximately 10 ms state of the art for diamond microscopes. Our microscope provides intrinsically calibrated polarization-resolved MW field images, with 130 nT Hz$^{-1/2}$ sensitivity, 48 dB dynamic range, and few-micron spatial resolution over an approximately 0.5 mm^2 FOV. In this work, we perform MW field imaging around 2.77–2.97 GHz; however, larger dc magnetic fields can be applied to tune the imaging frequency up to hundreds of gigahertz [16,39,40]. With the addition of a control MW field to perform dynamic decoupling, weak MW fields could be detected up to the $1/T_2$ limit [41,42]. With delta-doped NV surface layers, the spatial resolution could be further extended to the submicron range [24] or superresolution techniques could be employed to provide resolution down to the nanoscale [43,44]. We also identify ways to improve our fluorescence count rate, and thus the signal-to-noise ratio, by over 5 orders of magnitude (see SM Note 1 [30]).

Potential further applications of our high-temporal-resolution microscope include studies of MW device failure, changes in MW device operation with duty cycle, and the monitoring of integrated circuitry activity, e.g., logic processes on processor chips [22,45]. With the addition of a dc magnetic-field gradient, our microscope could operate as an analog MW spectrum analyzer [46], providing feedback on submillisecond timescales. MW electric-field imaging could be explored, detecting the electric field via Rabi oscillations driven on the electric transition coupling the $|\pm 1\rangle$ states [47], with a dc magnetic field used to

tune the $|\pm 1\rangle$ state splitting to resonance with the MW field. Widefield diamond microscopes hold promise for extending submicron widefield microscopy to MW medical imaging [8,9,11], which could enable new applications on the cellular level. With the use of a control MW field, materials analysis using scanning MW microscopy [10] could be extended to widefield imaging applications.

In addition to MW field imaging, there are a number of further modalities in which our microscope can be employed, including imaging spin waves in solid-state systems [6,7] to investigate, e.g., spin-transport waveguides based on ferromagnetic-domain walls [48] and as a possible alternative to Brillouin light-scattering techniques [49]. Using our 0.7 ms resolution, 2-point differential dc magnetic-field imaging can be performed at a 700 Hz rate. This is of interest, e.g., for the monitoring of biological processes such as neuron firing [50] and magnetic nanoparticle formation [51], and for microfluidics applications [52,53].

[1] Björn T. Rosner and Daniel W. Van Der Weide, High-frequency near-field microscopy, Rev. Sci. Instrum. **73,** 2505 (2002).

[2] Selahattin Sayil, D. V. Kerns, Jr., and S. E. Kerns, Comparison of contactless measurement and testing techniques to a all-silicon optical test and characterization method, IEEE Trans. Instrum. Meas. **54,** 2082 (2005).

[3] Andrew Horsley, PhD thesis, Department of Physics, University of Basel, Switzerland, 2015.

[4] B. Deutschmann, On the effects of transient electromagnetic interference on integrated circuits, Electron. Device Failure Anal. **8,** 16 (2006).

[5] Tristan Dubois, Sylvie Jarrix, Annick Penarier, Philippe Nouvel, Daniel Gasquet, Laurnet Chusseau, and Bruno Azais, Near-field electromagnetic characterization and perturbation of logic circuits, IEEE Trans. Instrum. Meas. **57,** 2398 (2008).

[6] Toeno van der Sar, Francesco Casola, Ronald Walsworth, and Amir Yacoby, Nanometre-scale probing of spin waves using single-electron spins, Nat. Commun. **6,** 7886 (2015).

[7] Chunhui Du, Toeno Van der Sar, Tony X. Zhou, Pramey Upadhyaya, Francesco Casola, Huiliang Zhang, Mehmet C. Onbasli, Caroline A. Ross, Ronald L. Walsworth, Yaroslav Tserkovnyak, and Amir Yacoby, Control and local measurement of the spin chemical potential in a magnetic insulator, Science **357,** 195 (2017).

[8] Natalia Nikolova, Microwave imaging for breast cancer, IEEE Microw. Mag. **12,** 78 (2011).

[9] Rohit Chandra, Huiyuan Zhou, Ilangko Balasingham, and Ram M. Narayanan, On the opportunities and challenges in microwave medical sensing and imaging, IEEE Trans. Biomed. Eng. **62,** 1667 (2015).

[10] C. Plassard, E. Bourillot, J. Rossignol, Y. Lacroute, E. Lepleux, L. Pacheco, and E. Lesniewska, Detection of defects buried in metallic samples by scanning microwave microscopy, Phys. Rev. B - Condens. Matter Mater. Phys. **83,** 2 (2011).

[11] Alexander Tselev, Jeyavel Velmurugan, Anton V. Ievlev, Sergei V. Kalinin, and Andrei Kolmakov, Seeing through walls at the nanoscale: Microwave microscopy of enclosed objects and processes in liquids, ACS Nano **10,** 3562 (2016).

[12] Pascal Böhi and Philipp Treutlein, Simple microwave field imaging technique using hot atomic vapor cells, Appl. Phys. Lett. **101,** 181107 (2012).

[13] Andrew Horsley, Guan-Xiang Du, Matthieu Pellaton, Christoph Affolderbach, Gaetano Mileti, and Philipp Treutlein, Imaging of relaxation times and microwave field strength in a microfabricated vapor cell, Phys. Rev. A **88,** 063407 (2013).

[14] Christoph Affolderbach, Guan-Xiang Du, Thejesh Bandi, Andrew Horsley, Philipp Treutlein, and Gaetano Mileti, Imaging microwave and DC magnetic fields in a vapor-cell Rb atomic clock, IEEE Trans. Instrum. Meas. **64,** 3629 (2015).

[15] Andrew Horsley, Guan-Xiang Du, and Philipp Treutlein, Widefield microwave imaging in alkali vapor cells with sub-100 μm resolution, New J. Phys. **17,** 112002 (2015).

[16] Andrew Horsley and Philipp Treutlein, Frequency-tunable microwave field detection in an atomic vapor cell, Appl. Phys. Lett. **108,** 211102 (2016).

[17] Haoquan Fan, Santosh Kumar, Jonathon Sedlacek, Harald Kübler, Shaya Karimkashi, and James P. Shaffer, Atom based RF electric field sensing, J. Phys. B **48,** 202001 (2015).

[18] Christopher L. Holloway, Matthew T. Simons, Joshua A. Gordon, Perry F. Wilson, Caitlyn M. Cooke, David A. Anderson, and Georg Raithel, Atom-based RF electric field metrology: From self-calibrated measurements to subwavelength and near-field imaging, IEEE Trans. Electromagn. Compat. **59,** 717 (2017).

[19] C. G. Wade, N. Šibalic, N. R. de Melo, J. M. Kondo, C. S. Adams, and K. J. Weatherill, Real-time near-field terahertz imaging with atomic optical fluorescence, Nat. Photonics **11,** 40 (2017).

[20] Pengfei Wang, Zhenheng Yuan, Pu Huang, Xing Rong, Mengqi Wang, Xiangkun Xu, Changkui Duan, Chenyong Ju, Fazhan Shi, and Jiangfeng Du, High-resolution vector microwave magnetometry based on solid-state spins in diamond, Nat. Commun. **6**, 6631 (2015).

[21] Patrick Appel, Marc Ganzhorn, Elke Neu, and Patrick Maletinsky, Nanoscale microwave imaging with a single electron spin in diamond, New J. Phys. **17**, 112001 (2015).

[22] Linbo Shao, Ruishan Liu, Mian Zhang, Anna V. Shneidman, Xavier Audier, Matthew Markham, Harpreet Dhillon, Daniel J. Twitchen, Yun-Feng Xiao, and Marko Lončar, Wide-field optical microscopy of microwave fields using nitrogen-vacancy centers in diamonds, Adv. Opt. Mater. **4**, 1075 (2016).

[23] K. Chang, A. Eichler, J. Rhensius, L. Lorenzelli, and C. L. Degen, Nanoscale imaging of current density with a single-spin magnetometer, Nano Lett. **17**, 2367 (2017).

[24] S. Steinert, F. Dolde, P. Neumann, A. Aird, B. Naydenov, G. Balasubramanian, F. Jelezko, and J. Wrachtrup, High sensitivity magnetic imaging using an array of spins in diamond, Rev. Sci. Instrum. **81**, 043705 (2010).

[25] David R. Glenn, Kyungheon Lee, Hongkun Park, Ralph Weissleder, Amir Yacoby, Mikhail D. Lukin, Hakho Lee, Ronald L. Walsworth, and Colin B. Connolly, Single-cell magnetic imaging using a quantum diamond microscope, Nat. Methods **12**, 736 (2015).

[26] D. A. Simpson, J. P. Tetienne, J. M. McCoey, K. Ganesan, L. T. Hall, S. Petrou, R. E. Scholten, and L. C. Hollenberg, Magneto-optical imaging of thin magnetic films using spins in diamond, Sci. Rep. **6**, 22797 (2016).

[27] D. R. Glenn, R. R. Fu, P. Kehayias, D. Le Sage, E. A. Lima, B. P. Weiss, and R. L. Walsworth, Micrometer-scale magnetic imaging of geological samples using a quantum diamond microscope, Geochem. Geophys. Geosyst. **18**, 3254 (2017).

[28] Jean-Philippe Tetienne, Nikolai Dontschuk, David A. Broadway, Alastair Stacey, David A. Simpson, and Lloyd C. L. Hollenberg, Quantum imaging of current flow in graphene, Sci. Adv. **3**, e1602429 (2017).

[29] Patrick Appel, Elke Neu, Marc Ganzhorn, Arne Barfuss, Marietta Batzer, Micha Gratz, Andreas Tschöpe, and Patrick Maletinsky, Fabrication of all diamond scanning probes for nanoscale magnetometry, Rev. Sci. Instrum. **87**, 063703 (2016).

[30] See the Supplemental Material at http://link.aps.org/supplemental/10.1103/PhysRevApplied.10.044039 for further details of the experiment and data analysis, and for movies of microwave magnetic fields captured by our microscope, which includes Refs. [54–63].

[31] M. Lesik, T. Plays, A. Tallaire, J. Achard, O. Brinza, L. William, M. Chipaux, L. Toraille, T. Debuisschert, A. Gicquel, J. F. Roch, and V. Jacques, Preferential orientation of NV defects in CVD diamond films grown on (113)-oriented substrates, Diam. Relat. Mater. **56**, 47 (2015).

[32] Marcus W. Doherty, Neil B. Manson, Paul Delaney, Fedor Jelezko, Jörg Wrachtrup, and Lloyd C. L. Hollenberg, The nitrogen-vacancy colour centre in diamond, Phys. Rep. **528**, 1 (2013).

[33] C. L. Degen, F. Reinhard, and P. Cappellaro, Quantum sensing, Rev. Mod. Phys. **89**, 035002 (2017).

[34] Pascal Böhi, Max F. Riedel, Theodor W. Hänsch, and Philipp Treutlein, Imaging of microwave fields using ultracold atoms, Appl. Phys. Lett. **97**, 051101 (2010).

[35] K. Sasaki, Y. Mannai, S. Saijo, R. Fujita, H. Watanabe, J. Ishi-Hayase, K. Itoh, and E. Abe, Broadband, large-area microwave antenna for optically detected magnetic resonance of nitrogen-vacancy centers in diamond, Rev. Sci. Instrum. **87**, 053904 (2016).

[36] Jakob Reichel, and Vuletic Vladan, eds., *Atom Chips* (Wiley-Blackwell VCH, Weinheim, Germany, 2011).

[37] R. J. C. Spreeuw, C. Gerz, Lori S. Goldner, W. D. Phillips, S. L. Rolston, C. I. Westbrook, M. W. Reynolds, and Isaac F. Silvera, Demonstration of Neutral Atom Trapping with Microwaves, Phys. Rev. Lett. **72**, 3162 (1994).

[38] Pascal Böhi, Max F. Riedel, Johannes Hoffrogge, Jakob Reichel, Theodor W. Hänsch, and Philipp Treutlein, Coherent manipulation of Bose-Einstein condensates with state-dependent microwave potentials on an atom chip, Nat. Phys. **5**, 592 (2009).

[39] Viktor Stepanov, Franklin H. Cho, Chathuranga Abeywardana, and Susumu Takahashi, High-frequency and high-field optically detected magnetic resonance of nitrogen-vacancy centers in diamond, Appl. Phys. Lett. **106**, 063111 (2015).

[40] Nabeel Aslam, Matthias Pfender, Rainer Stöhr, Philipp Neumann, Marc Scheffler, Hitoshi Sumiya, Hiroshi Abe, Shinobu Onoda, Takeshi Ohshima, Junichi Isoya, and Jörg Wrachtrup, Single spin optically detected magnetic resonance with 60–90 GHz (E-band) microwave resonators, Rev. Sci. Instrum. **86**, 064704 (2015).

[41] T. Joas, A. M. Waeber, G. Braunbeck, and F. Reinhard, Quantum sensing of weak radio-frequency signals by pulsed Mollow absorption spectroscopy, Nat. Commun. **8**, 964 (2017).

[42] Alexander Stark, Nati Aharon, Thomas Unden, Daniel Louzon, Alexander Huck, Alex Retzker, Ulrik Lund Andersen, and Fedor Jelezko, Narrow-bandwidth sensing of high-frequency fields with continuous dynamical decoupling, Nat. Commun. **8**, 1105 (2017).

[43] Edward H. Chen, Ophir Gaathon, Matthew E. Trusheim, and Dirk Englund, Wide-field multispectral super-resolution imaging using spin-dependent fluorescence in nanodiamonds, Nano Lett. **13**, 2073 (2013).

[44] K. Arai, C. Belthangady, H. Zhang, N. Bar-Gill, S. J. DeVience, P. Cappellaro, A. Yacoby, and R. L. Walsworth, Fourier magnetic imaging with nanoscale resolution and compressed sensing speed-up using electronic spins in diamond, Nat. Nanotechnol. **10**, 859 (2015).

[45] A. Nowodzinski, M. Chipaux, L. Toraille, V. Jacques, J. F. Roch, and T. Debuisschert, Nitrogen-vacancy centers in diamond for current imaging at the redistributive layer level of integrated circuits, Microelectron. Reliab. **55**, 1549 (2015).

[46] M. Chipaux, L. Toraille, C. Larat, L. Morvan, S. Pezzagna, J. Meijer, and T. Debuisschert, Wide bandwidth instantaneous radio frequency spectrum analyzer based on nitrogen vacancy centers in diamond, Appl. Phys. Lett. **107**, 233502 (2015).

[47] A. Barfuss, J. Teissier, E. Neu, A. Nunnenkamp, and P. Maletinsky, Strong mechanical driving of a single electron spin, Nat. Phys. **11,** 820 (2015).

[48] Felipe Garcia-Sanchez, Pablo Borys, Rémy Soucaille, Jean-paul Adam, Robert L. Stamps, and Joo Von Kim, Narrow Magnonic Waveguides based on Domain Walls, Phys. Rev. Lett. **114,** 247206 (2015).

[49] Thomas Sebastian, Katrin Schultheiss, Björn Obry, Burkard Hillebrands, and Helmut Schultheiss, Micro-focused Brillouin light scattering: Imaging spin waves at the nanoscale, Front. Phys. **3,** 35 (2015).

[50] L. T. Hall, G. C. G. Beart, E. A. Thomas, D. A. Simpson, L. P. McGuinness, J. H. Cole, J. H. Manton, R. E. Scholten, F. Jelezko, Jörg Wrachtrup, S. Petrou, and L. C. L. Hollenberg, High spatial and temporal resolution wide-field imaging of neuron activity using quantum NV-diamond, Sci. Rep. **2,** 401 (2012).

[51] D. Le Sage, K. Arai, D. R. Glenn, S. J. DeVience, L. M. Pham, L. Rahn-Lee, M. D. Lukin, A. Yacoby, A. Komeili, and R. L. Walsworth, Optical magnetic imaging of living cells, Nature **496,** 486 (2013).

[52] Li Yao and Shoujun Xu, Detection of magnetic nanomaterials in molecular imaging and diagnosis applications, Nanotechnol. Rev. **3,** 247 (2014).

[53] D. Issadore, Y. I. Park, H. Shao, C. Min, K. Lee, M. Liong, R. Weissleder, and H. Lee, Magnetic sensing technology for molecular analyses, Lab Chip **14,** 2385 (2014).

[54] Michael S. J. Barson, Phani Peddibhotla, Preeti Ovartchaiyapong, Kumaravelu Ganesan, Richard L. Taylor, Matthew Gebert, Zoe Mielens, Berndt Koslowski, David A. Simpson, Liam P. McGuinness, Jeffrey McCallum, Steven Prawer, Shinobu Onoda, Takeshi Ohshima, Ania C. Bleszynski Jayich, Fedor Jelezko, Neil B. Manson, and Marcus W. Doherty, Nanomechanical sensing using spins in diamond, Nano Lett. **17,** 1496 (2017).

[55] Bradley J. Roth, Nestor G. Sepulveda, and John P. Wikswo, Jr., Using a magnetometer to image a two-dimensional current distribution, J. Appl. Phys. **65,** 361 (1989).

[56] D. Budker and M. Romalis, Optical magnetometry, Nat. Phys. **3,** 227 (2007).

[57] Nico Stuurman, Arthur D. Edelstein, Nenad Amodaj, Karl H. Hoover, and D. Ronald, Computer control of microscopes using μ manager, Curr. Protoc. Mol. Biol. **92,** 14.20.1 (2010).

[58] Arthur D. Edelstein, Mark A. Tsuchida, Nenad Amodaj, Henry Pinkard, Ronald D. Vale, and Nico Stuurman, Advanced methods of microscope control using μ manager software, J. Biol. Methods **1,** 10 (2014).

[59] Hannah Clevenson, Matthew E. Trusheim, Tim Schröder, Carson Teale, Danielle Braje, and Dirk Englund, Broadband magnetometry and temperature sensing with a light trapping diamond waveguide, Nat. Phys. **11,** 393 (2015).

[60] R. Hanson, V. V. Dobrovitski, A. E. Feiguin, O. Gywat, and D. D. Awschalom, Coherent dynamics of a single spin interacting with an adjustable spin bath, Science **320,** 352 (2008).

[61] A. Dréau, M. Lesik, L. Rondin, P. Spinicelli, O. Arcizet, J. F. Roch, and V. Jacques, Avoiding power broadening in optically detected magnetic resonance of single NV defects for enhanced dc magnetic field sensitivity, Phys. Rev. B **84,** 195204 (2011).

[62] Rich Mildren, and James Rabeau, eds., *Optical Engineering of Diamond* (Wiley-VCH, Weinheim, Germany, 2013).

[63] Jacques Vanier, Claude Audoin, and Adam Hilger, *The Quantum Physics of Atomic Frequency Standards* (Adam Hilger, Bristol, 1989), Vol. 1.